Large magneto-optical Kerr effect and imaging of magnetic octupole domains in an antiferromagnetic metal

Tomoya Higo[1,2], **Huiyuan Man**[1], **Daniel B. Gopman**[3], **Liang Wu**[4,5,6], **Takashi Koretsune**[2,7,8], **Olaf M. J. van 't Erve**[9], **Yury P. Kabanov**[3,10], **Dylan Rees**[4,5], **Yufan Li**[11], **Michi-To Suzuki**[2,8], **Shreyas Patankar**[4,5], **Muhammad Ikhlas**[1,2], **C. L. Chien**[11], **Ryotaro Arita**[2,8], **Robert D. Shull**[3], **Joseph Orenstein**[4,5], and **Satoru Nakatsuji**[1,2,*]

[1]Institute for Solid State Physics, University of Tokyo, Kashiwa, Chiba 277-8581, Japan

[2]CREST, Japan Science and Technology Agency, Kawaguchi, Saitama 332-0012, Japan

[3]Materials Science and Engineering Division, National Institute of Standards and Technology, Gaithersburg, MD 20899, USA

[4]Department of Physics, University of California, Berkeley, California 94720, USA

[5]Materials Science Division, Lawrence Berkeley National Laboratory, Berkeley, California 94720, USA

[6]Department of Physics and Astronomy, University of Pennsylvania, Philadelphia, Pennsylvania 19104, USA

[7]Department of Physics, Tohoku University, Sendai, Miyagi 980-8578, Japan

[8]RIKEN-CEMS, Wako, Saitama 351-0198, Japan

[9]Materials Science and Technology Division, U.S. Naval Research Laboratory, Washington, DC 20375, USA

[10]Institute of Solid State Physics, Russian Academy of Sciences, Chernogolovka, Moscow Region 142432, Russia

[11]Department of Physics and Astronomy, Johns Hopkins University, Baltimore, MD 21218, USA

Abstract

When a polarized light beam is incident upon the surface of a magnetic material, the reflected light undergoes a polarization rotation[1]. This magneto-optical Kerr effect (MOKE) has been intensively studied in a variety of ferro- and ferrimagnetic materials because it provides a powerful probe for

electronic and magnetic properties[2, 3] as well as for various applications including magneto-optical recording[4]. Recently, there has been a surge of interest in antiferromagnets (AFMs) as prospective spintronic materials for high-density and ultrafast memory devices, owing to their vanishingly small stray field and orders of magnitude faster spin dynamics compared to their ferromagnetic counterparts[5–9]. In fact, the MOKE has proven useful for the study and application of the antiferromagnetic (AF) state. Although limited to insulators, certain types of AFMs are known to exhibit a large MOKE, as they are weak ferromagnets due to canting of the otherwise collinear spin structure[10–14]. Here we report the first observation of a large MOKE signal in an AF metal at room temperature. In particular, we find that despite a vanishingly small magnetization of M ~0.002 μ_B/Mn, the non-collinear AF metal Mn_3Sn[15] exhibits a large zero-field MOKE with a polar Kerr rotation angle of 20 milli-degrees, comparable to ferromagnetic metals. Our first-principles calculations have clarified that ferroic ordering of magnetic octupoles in the non-collinear Néel state[16] may cause a large MOKE even in its fully compensated AF state without spin magnetization. This large MOKE further allows imaging of the magnetic octupole domains and their reversal induced by magnetic field. The observation of a large MOKE in an AF metal should open new avenues for the study of domain dynamics as well as spintronics using AFMs.

The magneto-optical (MO) Kerr and Faraday effects in ferro- and ferrimagnets arise from the combined effects of band exchange splitting and spin-orbit interactions (SOI)[17–19] and are powerful probes of the local magnetization in such materials. In the case of antiferromagnets (AFMs), observation of the MOKE has been restricted to a certain class of insulators (e.g. orthoferrites and iron borate)[9–13, 20–22], which have weak ferromagnetism due to canting of the otherwise collinear Néel order. In the fully compensated collinear AFMs, where the MOKE is usually absent, the quadratic MO effects such as the Voigt effect can be useful to determine the Néel vector[23].

On the other hand, recent theoretical and experimental progress has revealed that systems such as certain spin liquids and non-collinear antiferromagnets may exhibit a large Hall response in zero applied magnetic field (anomalous Hall effect or AHE) despite a vanishing magnetization[15, 24–30]. Because the AHE has the same symmetry requirements as the MOKE[31], it is possible that the same class of antiferromagnets may exhibit a Kerr rotation. Thus, the recent experimental discovery of a large AHE in the non-collinear antiferromagnet Mn_3Sn and its soft response to a magnetic field[15] give promise for a potentially large MOKE character.

Mn_3Sn is a hexagonal antiferromagnet (space group P6$_3$/mmc)[32], which has the ABAB stacking sequence of the (0001)-plane consisting of a kagome lattice of Mn magnetic moments. Below the Néel temperature T_N ~430 K, the combination of inter-site AF and Dzyaloshinskii-Moriya (DM) interactions leads to an inverse triangular spin structure, namely, a 120 degree spin structure with a uniform negative vector chirality of the in-plane Mn moments because of geometrical frustration (Figure 1a)[15, 32, 33]. Significantly, this three-sublattice AF state on the kagome bilayers can be viewed as ferroic ordering of cluster magnetic octupoles (Fig. 1a)[16]. In addition to this dominant order parameter, the moments cant slightly in the plane to produce a small net ferromagnetic (FM) moment of ~0.002 μ_B/Mn along the local easy axis in the (0001)-plane, e.g. [2$\bar{1}\bar{1}$0] and [01$\bar{1}$0][15]. This small

moment, which corresponds to less than 10^{-3} of the local Mn moment, is theoretically understood to result from the competition between the DM interaction and single-ion anisotropy[34]. Although, as we discuss below, the sub-dominant FM order is not responsible for the AHE and MOKE, it is essential (together with concomitant weak in-plane anisotropy) for magnetic field control of the AF spin structure. This control is demonstrated, for example, by the ability to reverse the sign of the AHE by application of a small applied field of $B \sim 15$ mT within the (0001)-plane, which is sufficient to reverse the direction of the Mn moments[15].

Before presenting the main MOKE results, we shall first discuss the AHE and magnetization curve. In this study, we used as-grown single crystals with the composition of $Mn_{3.06}Sn_{0.94}$ (Methods) and confirmed no magnetic transition above 50 K[15]. Figures 1c and 1d provide the field dependence of the Hall resistivity $\rho_H(B)$ and magnetization $M(B)$ for $B \parallel [2\bar{1}\bar{1}0]$ at room temperature (RT), respectively (Methods). The observed $\rho_H(B = 0) = 3.1$ μΩcm is large and is equivalent to the size of the ordinary Hall effect under an external field of ~100 T estimated using the Hall coefficient of $R_0 \sim 0.03$ μΩcm/T[15]. This sizable $\rho_H(B = 0)$ with vanishingly small spontaneous M strongly suggests another form of order rather than FM (in this case magnetic octupole) is responsible for the AHE[15, 16, 24].

Now, we turn to our results of the MOKE measurements. Similar to the AHE experiments, we carried out field-swept measurements of the polar MOKE using the Mn_3Sn $(2\bar{1}\bar{1}0)$-plane with a $\lambda = 660$ nm semiconductor laser at 300 K (Methods, Fig. 1b). Significantly, a large change of the Kerr rotation angle $|\theta_K| = 17.5$ milli-degrees and a clear square hysteresis loop are observed as a function of the field $B \parallel [2\bar{1}\bar{1}0]$ (Fig. 2a). The coercive field of $B_C \sim 12$ mT is consistent with the hysteresis curve obtained in $\rho_H(B)$, indicating that the magnetic properties at the surface are nominally identical to those in the bulk. The MOKE in an AF metal is unprecedented. Figure 2b provides the longitudinal MOKE loops measured in various B directions within the $(2\bar{1}\bar{1}0)$-plane at 300 K (Methods). Upon changing the direction of both the applied field B and plane of incidence from $[01\bar{1}0]$ ($\varphi = 0°$) to $[0001]$ ($\varphi = 90°$) in the $(2\bar{1}\bar{1}0)$-plane (Fig. 2c), we find that the MOKE signal decreases and the coercivity increases. Finally, the MOKE signal disappears when B and the plane of incidence are parallel to the magnetic hard axis $[0001]$ ($\varphi = 90°$). The signal magnitude is proportional to the projection of B onto $[01\bar{1}0]$, which demonstrates that the surface magnetic character probed by the MOKE is consistent with our previous studies on bulk transport and magnetization[15]. We also performed polar MOKE spectroscopy on the same sample with the wavelength from 400 nm to 1100 nm at 300 K (Methods). In Fig. 2d, we plot the spontaneous Kerr rotation $\theta_K(B = 0) = (\theta_{K,+0T} - \theta_{K,-0T})/2$, which removes time-reversal even effects such as birefringence resulting from structural anisotropy and the Voigt effect, and illustrates the history dependent remnant response. The spectra show a broad peak with magnitude 19.6 milli-degrees at $\lambda = 580$ nm (2.1 eV).

A striking property of the MOKE data is that, once application of a small magnetic field serves to rotate the spin orientation, further increase of the field and therefore the magnetization, does not affect much on the size of the Kerr effect (Fig. 1d and Fig. 2a). This observation strongly suggests that the amplitude of the MOKE and the FM magnetization are entirely decoupled in this system. As a result, the ratio of the MOKE amplitude to M is

unusually large. To emphasize this point, we compare the polar MOKE in Mn_3Sn with values reported for ferro- and ferrimagnets and AF insulators. Figure 3 is a double-logarithmic plot of the polar MOKE signal vs. magnetization (Methods) obtained at RT. The wavelengths used in the various measurements are all in the range between 250 nm and 1250 nm. For FM systems, there is a clear trend that the Kerr angle increases with the magnetization. This is consistent with the theoretical expectation that the MOKE is roughly proportional to M (and SOI)[17]. However, this correlation is not as straightforward as is the case for the AHE[24, 35] because the MOKE can exhibit a complicated frequency dependence including sign changes. Nonetheless, we note that the ratio $|\theta_K|/M = 25.6$ degrees/T of Mn_3Sn is largest among all the empirical reports, i.e. 1–2 order(s) of magnitude larger than ferro- and ferrimagnets, and still the largest among those known for canted AF insulators that have a similar magnitude to Mn_3Sn.

The experimental evidence presented above for the decoupling of the MOKE from the FM order is strongly supported by theoretical considerations. Detailed symmetry analysis[16] demonstrated that, despite vanishing M, ferroic octupole order was sufficient to induce a non-zero net Berry curvature of the Fermi sea, and hence an AHE. Further it was demonstrated that the size of the AHE in Mn_3Sn could be reproduced in a model in which the spin orientations are set such that $M = 0$. As the AHE corresponds to the $\omega \rightarrow 0$ limit of the MOKE, the same symmetry considerations apply to both. To further test the connection of this theory to experiment, we have performed a first-principles calculation of the frequency dependence of the Kerr rotation $\theta_K(\omega)$ for the fully compensated AF state without spin canting for Mn_3Sn (Methods). The calculation reproduces the large Kerr rotation of ~30 milli-degrees at around 520 nm (2.4 eV) (Fig. 2d inset), which corresponds to the observed value of ~20 milli-degrees at 580 nm (2.1 eV). Our results of a large MOKE *without* spin magnetization sharply contrast with the previously known AF insulator cases where weak ferromagnetism has been believed to be essential for the presence of the MOKE[11, 12, 36]. In addition, we find almost no change in the Kerr angle by increasing M from 0 to 0.005 μ_B/ formula unit (f.u.) (Fig. 2d inset). In contrast, the change in the size of the octupole, which is proportional to the sublattice moment, should lead to a significant change in the band structure and AHE[16], and hence in the MOKE. Therefore, in Mn_3Sn, it is not magnetization but magnetic octupole that induces the large MOKE. Further reflectivity measurements using e.g. Fourier-transform infrared spectroscopy will be useful to clarify $\sigma_{ij}(\omega)$ and will help understand the origin of the MOKE in the AF metallic state.

Having shown the sizable Kerr rotation in Mn_3Sn, we demonstrate the application of the MOKE microscopy as a useful non-contact and non-destructive probe for imaging of magnetic domains and their corresponding dynamics. In particular, we apply the polar MOKE to visualize the magnetic domains in the AF state of Mn_3Sn (Methods). A series of MOKE images of the Mn_3Sn ($2\bar{1}\bar{1}0$)-plane under $B \parallel [2\bar{1}\bar{1}0]$ (−21 mT B 21 mT) are presented in Figs. 4a to 4h. Changes in contrast from grey-to-black and black-to-grey are evident over the sequence of increasing field (Figs. 4a–d) and decreasing field (Figs. 4e–4h), respectively. Here, the grey and black colours correspond to positive and negative values of the polar MOKE signal $\parallel [2\bar{1}\bar{1}0]$. As discussed above, the symmetry considerations show that switching of the magnetic octupole domains with a triangular spin texture can flip the sign of $\sigma_{ij}(\omega)$ and consequently the Kerr angle θ_K. Particularly in $B \parallel [2\bar{1}\bar{1}0]$, one of the

three moments of a Mn triangle aligns with the field, with the other two at ± 120 degrees away (Fig. 1a). Therefore, the grey and black regions are interpreted as the domains in which the Mn spin collinear with the field (the magnetic octupolar axis) points either along the positive or negative $[2\bar{1}\bar{1}0]$ direction (Fig. 4i). Provided that the in-plane Mn moments have an easy-axis along $[2\bar{1}\bar{1}0]$, Mn_3Sn may have six types of domains in principle, corresponding to six equivalent axes to $\langle 2\bar{1}\bar{1}0 \rangle$ in the (0001)-plane. However, a clear square shape observed in our MOKE hysteresis loop, AHE and magnetization measurements for $B \parallel [2\bar{1}\bar{1}0]$ (Figs. 1 and 2) all suggest that the field cycle only stabilizes the two types of the magnetic octupole domains shown in Fig. 4i. Indeed, only two distinct regions with different colours are found in Figs. 4b, c, f and g.

Generally, in ferromagnets, two fundamental processes in the magnetization reversal are known, namely, (i) reversal by domain nucleation and domain wall propagation, and (ii) reversal by coherent rotation. The series of our domain images indicates the former mechanism while the coarse resolution hinders the observation of nucleation itself. At the highest field $B = 18.4$ mT (Fig. 4d), the view of the entire region (25 μm × 50 μm) reflects an oppositely aligned domain in contrast to the initial domain configuration (Fig. 4a). Similar evolution of the domain images is obtained for the field-increasing and -decreasing processes (Fig. 4). Interestingly, the domain images around zero field in the field-increasing (Fig. 4a) and -decreasing processes (Fig. 4e) show grey/black contrast, respectively, confirming that these mono-domains have a spontaneous Kerrangle at zero field whose sign can be switched by a modest coercive field ~10 mT. This is the first observation of the domain reversal in an AF metal and the magnetic octupole domain reversal by MOKE microscopy.

The observation of the large MOKE signal and the magnetic octupole domain reversal in the antiferromagnet Mn_3Sn has various implications. In spintronics, antiferromagnets have attracted significant attention as a potential active element in the next generation memory technology[5–9]. The MOKE in AF metals may well accelerate the development of future memory devices with emergent optical, magnetic and electric properties by taking advantage of significantly large reflectivity in comparison with insulators. Furthermore, our success in the magneto-optical imaging of the domain configurations in an AF metal opens a new avenue for studying current-driven domain dynamics. In principle, the AF domain dynamics could be very different from the ones in ferromagnets as the magneto-static energy, which is the primary driving force of the domain formation in ferromagnets, is unimportant in antiferromagnets. In particular in Mn_3Sn, six magnetic domains and the associated various types of topological defects could be possible including a vortex type of point defect around which the six domains meet. It is a future subject to investigate the possible current-induced AF domain wall motion[37]. Finally, the topological aspect of the magnetic state (magnetic Weyl state) of Mn_3Sn, which has been recently pointed out by theoretical[38] and experimental[39] studies, would make it interesting to investigate the Berry curvature effects in the MOKE at low frequency, and further make the topological defects even more attractive as the bulk-edge correspondence for such a magnetic Weyl semimetallic state may lead to a Fermi arc in a magnetic domain wall, and contribute to the MOKE signal in an unconventional fashion[37, 40].

Methods

Sample preparation and characterization

Polycrystalline samples were prepared by melting the mixtures of manganese and tin in an alumina crucible sealed in an evacuated quartz ampoule in a box furnace at 1050 °C for 6 hours. Excess manganese (10 mol.%) over the stoichiometric amount was added to compensate for its loss during crystal growth. The obtained polycrystalline materials were used for growing single crystals by the Bridgman method using a single zone furnace with a maximum temperature of 1080 °C and growth speed of 1.5 mm/h. Our single-crystal and powder x-ray measurements indicate the presence of only single phase hexagonal Mn_3Sn with the lattice constants of $a = 5.66(1)$ Å and $c = 4.53(1)$ Å. Our scanning electron microscopy energy dispersive x-ray spectroscopy (SEM-EDX) and inductively coupled plasma atomic emission spectrometry (ICP-AES) analyses confirmed that Mn_3Sn is the bulk phase, and found that the composition of the single crystals is $Mn_{3.06}Sn_{0.94}$. The magnetization was measured using a commercial SQUID magnetometer (MPMS, Quantum Design). The Hall resistivity was measured by a standard four-probe method using a commercial physical property measurement system (PPMS, Quantum Design). Our as-grown single crystals are found to exhibit a phase transition to a cluster glass phase at 50 K[15]. In this study, we used as-grown single crystals that show no transition above 50 K.

Magnetic field dependence of the magneto-optical Kerr effect (MOKE) shown in Figs. 2a, 2b, & 2c

Magnetic field dependence of the Magneto-optical Kerr effect (MOKE) was measured by using a commercial system (NanoMOKE3, Quantum Design). Bulk Mn_3Sn crystals were used for the MOKE spectroscopy measurement. Crystal samples were cut and polished so that the samples had optically smooth surfaces along the $(2\bar{1}\bar{1}0)$-plane. Kerr rotation versus applied field were measured in a polar MOKE configuration under out-of-plane applied magnetic fields, and in a longitudinal MOKE configuration under in-plane applied magnetic fields. In the polar MOKE configuration, a polarized light beam and magnetic field are applied perpendicular to the reflecting $(2\bar{1}\bar{1}0)$-plane. The plane of the input polarization is parallel to the [0001] direction. In the longitudinal MOKE configuration, the magnetic field is parallel to both the plane of incidence and the reflecting surface. The polarized light beam is applied under an incident angle of 45 degrees and the plane of polarization is parallel to the plane of the incidence. φ is the angle between the plane of incidence/magnetic field and the $[01\bar{1}0]$ direction. An electromagnet was used to generate both in-plane and out-of-plane applied magnetic fields up to 0.24 T. Fast MOKE loops were acquired using a 660 nm semiconductor laser and a spatial light modulator (SLM) enabling acquisition of 30 hysteresis loops per minute while the applied field was sinusoidally varied at a rate of 0.5 Hz. One hundred MOKE loops were averaged in order to improve the signal to noise fidelity. To obtain the MOKE signal, which is an odd function of magnetic field B (more precisely magnetization M and/or ferroic octupole order parameter in Mn_3Sn), we calculated the Kerr rotation to be $\{\theta_K(+B) - \theta_K(-B)\}/2$.

Magneto-optical Kerr effect (MOKE) spectroscopy shown in Fig. 2d

Magneto-optical Kerr effect spectroscopy was performed by using a W-filament light source and grating monochromator. The $(2\bar{1}\bar{1}0)$-polished Mn_3Sn single crystal was used for the measurement as with the MOKE hysteresis loop measurement. In a polar Kerr measurement, linearly polarized light was focused onto the sample with a ~10 μm diameter spot by a reflective objective with an incidence angle close to normal and the reflected light was collected by a pick-up mirror. To measure the Kerr rotation, we used a technique based on a photoelastic optical phase modulator (PEM)[41, 42]. Synchronous detection of the reflected light at the second harmonic of the PEM frequency and DC reflectivity enabled precision of rotation with 0.25 milli-degrees (5 μrad) sensitivity. The plane of the input polarization is parallel to the [0001] direction. Spectra were acquired for the following sequence of fields: +0.2 T (with respect to $[2\bar{1}\bar{1}0]$), +0 T, −0.2 T, and then finally −0 T again. We refer to the zero field condition following ±0.2 T as ±0 T. The spectra exhibit the same hysteretic and remnant behaviour as the AHE and single wavelength MOKE observations. In particular, Kerr rotation is observed at 0.2 T, remains unchanged at +0 T, flips sign when measured at −0.2 T, and then remains at −0 T with opposite sign to the MOKE signal at +0 T. In Fig. 2d, we plot the spontaneous magneto-optical Kerr rotation $\theta_K(B = 0) = (\theta_{K,+0T} − \theta_{K,−0T})/2$, where $\theta_{K,\pm0T}$ is the Polar Kerr angle at ±0 T. This estimate of $\theta_K(B = 0)$ removes time-reversal even effects such as birefringence resulting from structural anisotropy and the Voigt effect, and illustrates the history dependent remnant response.

Magneto-optical Kerr effect (MOKE) imaging shown in Fig. 4

For magneto-optical imaging of the magnetic domain configurations in bulk Mn_3Sn crystals, the same $(2\bar{1}\bar{1}0)$-polished sample, which was used in the MOKE hysteresis loop and spectroscopy measurements, was used. The magneto-crystalline anisotropy tends to align the magnetization along the $[2\bar{1}\bar{1}0]$ direction, which enables us to conduct polar MOKE investigation of the out-of-plane magnetic domains in the $(2\bar{1}\bar{1}0)$-plane. Magneto-optical imaging was performed at room temperature using a polarizing microscope with nearly-crossed polarizers and a 625 nm collimated LED source. Direct visualization of out-of-plane domain structures was provided during the domain-reversal process using the polar magneto-optical Kerr effect. The black and grey colours of the magneto-optical image correspond to opposite signs of the magnetic domain direction. Magneto-optical imaging was made using a charge coupled device (CCD) camera. Applied out-of-plane magnetic fields were generated by a projected-field electromagnet, enabling the application of magnetic fields up to 21 mT (16.8 kA/m) in magnitude. Certain equipment, instruments or materials are identified in this paper in order to adequately specify the experimental details. Such identification does not imply recommendation by the endorsement by the authors or their organizations nor does it imply the materials are necessarily the best available for the purpose.

Computational details

Under the magnetic structure shown in Fig. 1a, the conductivity tensor has the form

$$\boldsymbol{\sigma} = \begin{pmatrix} \sigma_{xx} & 0 & 0 \\ 0 & \sigma_{yy} & \sigma_{yz} \\ 0 & -\sigma_{yz} & \sigma_{zz} \end{pmatrix}, \quad (1)$$

where x, y, and z correspond to $[2\bar{1}\bar{1}0]$, $[01\bar{1}0]$, and $[0001]$ directions, respectively. Here, $\sigma_{\alpha\beta}$ is approximated using the Kubo formula as

$$\sigma_{\alpha\beta}(\hbar\omega) = \frac{ie^2\hbar}{N_k\Omega_c} \sum_{k,n,m} \frac{f(\varepsilon_{mk}) - f(\varepsilon_{nk})}{\varepsilon_{mk} - \varepsilon_{nk}} \frac{\langle\psi_{nk}|v_\alpha|\psi_{mk}\rangle\langle\psi_{mk}|v_\beta|\psi_{nk}\rangle}{\varepsilon_{mk} - \varepsilon_{nk} - (\hbar\omega + i\eta)}, \quad (2)$$

where Ω_c is the cell volume, N_k is the number of k-points, $f(\varepsilon)$ is the Fermi distribution function, and η is the smearing parameter. Since the incident light is along the x-axis, the polar Kerr effect can be described by the two eigen modes, $\boldsymbol{E}_\pm$ and corresponding complex refractive indices, $n_\pm$. Here, $\boldsymbol{E}_\pm$ and $n_\pm$ are the solutions of the Fresnel equation for Eq. (1) and given as

$$n_\pm^2 = 1 + \frac{4\pi i}{\omega}\left(\frac{\sigma_{yy} + \sigma_{zz}}{2} \pm \sqrt{\frac{1}{4}(\sigma_{yy} - \sigma_{zz})^2 - \sigma_{yz}^2}\right). \quad (3)$$

Then, by decomposing the linearly polarized incident light, $\boldsymbol{E}_z$, as $\boldsymbol{E}_z = p\boldsymbol{E}_+ + q\boldsymbol{E}_-$, the reflected light is written as

$$p\frac{n_+ - 1}{n_+ + 1}\boldsymbol{E}_+ + q\frac{n_- - 1}{n_- + 1}\boldsymbol{E}_-. \quad (4)$$

Thus, by analyzing the orientation of the ellipse of this light, the Kerr rotation, θ_K is obtained. For calculating Eq. (2), the Kohn-Sham energy, ε_{nk}, and wavefunction, $|\psi_{nk}\rangle$, were obtained within the generalized-gradient approximation[43] based on the density functional theory as implemented in the quantum-ESPRESSO package[44]. A $7 \times 7 \times 7$ k-point grid, ultrasoft pseudopotentials[45] and plane wave basis sets with cutoff energies of 80 Ry for wavefunctions and 320 Ry for charge densities were used. The obtained magnetic moment for each Mn atom is 3.26 μ_B while the total magnetic moment vanishes due to cancellation within the numerical error. We also performed calculation with constraint on M and calculated θ_K for $M = 0.005$ and 0.025 μ_B/f.u.. The summation in Eq. (2) were taken using a Wannier-interpolated band structure[46] with a $50 \times 50 \times 50$ k-point grid and a smearing width of $\eta = 0.4$ eV.

Detailed information about MOKE results for ferro- and ferrimagnets, and antiferromagnetic insulators shown in Fig. 3

Figure 3 is made using the polar MOKE results obtained at room temperature (RT) from various (i) ferro- and ferrimagnetic metals, (ii) ferro- and ferrimagnetic insulators, and (iii) antiferromagnetic insulators, as reported in previous studies including (i) $L1_0$-Mn_xGa_{1-x}: $0.43 \leq x \leq 0.56$ ($\lambda = 670$ nm, $T = 300$ K)[47, 48] and $x = 0.62$ (820 nm, RT)[49], $L1_2$-Mn_3Pt (650 and 1000 nm, RT)[50], $MnBi$ (700 and 900 nm, RT)[51], $MnSb_{1-x}Sn_x$: $0 \leq x \leq 0.4$ (633 nm, RT)[52], and $MnAlGe$ (633 nm, RT)[53], $PtMnSb$ (710 nm, RT)[54], Ni (633 nm, RT)[53], Co (633 nm, RT)[53], Co_xGa_{1-x}: $0.58 \leq x \leq 0.7$ (633 nm, RT)[53], Co_2Sn (633 nm, RT)[53], Fe (633 nm, RT)[53], Fe_xAl_{1-x}: $0.7 \leq x \leq 0.9$ (633 nm, RT)[53], Fe_xGa_{1-x}: $0.6 \leq x \leq 0.8$ (633 nm, RT)[53], Fe_xGe_{1-x}: $x = 0.85$ and 0.9 (633 nm, RT)[53], $D0_{19}$-Fe_3Ge (633 nm, RT)[53], $D0_{19}$-Fe_3Sn (633 nm, RT)[53], $MnSb_xSn_{1-x}$: $0 \leq x \leq 0.4$ (633 nm, RT)[52], and $L1_0$-$FePt$ (633 nm, RT)[55], and (ii) Fe_3O_4 (1240 nm, RT)[56], $Y_3Fe_5O_{12}$ (251 nm, RT)[10, 57], $Eu_3Fe_5O_{12}$ (253 nm, RT)[57, 58], $Ho_3Fe_5O_{12}$ (279 nm, RT)[57, 59], and $Er_3Fe_5O_{12}$ (251 nm, RT)[10, 57], and (iii) $YFeO_3$ (421 nm, RT)[10, 60], $SmFeO_3$ (430 nm, RT)[10, 61], $EuFeO_3$ (432 nm, RT)[10, 60], $DyFeO_3$ (324 nm, RT)[10, 60], $ErFeO_3$ (320 nm, RT)[10, 61], $YbFeO_3$ (328 nm, RT)[10, 61], $LuFeO_3$ (324 nm, RT)[10, 61].

The data that support the plots within this paper and other findings of this study are available from the corresponding author upon reasonable request.

Acknowledgments

References

1. Kerr J. On rotation of the plane of the polarization by reflection from the pole of a magnet. Philos. Mag. 1877; 3:321–343.

2. Zvezdin, AK., Kotov, VA. Modern Magnetooptics and Magnetooptical Materials. Institute of Physics; 1997.

3. McCord J. Progress in magnetic domain observation by advanced magneto-optical microscopy. J. Phys. D: Appl. Phys. 2015; 48:333001.

4. Mansuripur, M. The Physical Principles of Magneto-Optical Recording. Cambridge University; New York: 1995.

5. MacDonald AH, Tsoi M. Antiferromagnetic metal spintronics. Phil. Trans. R. Soc. A. 2011; 369:3098–3114. [PubMed: 21727116]

6. Gomonay EV, Loktev VM. Spintronics of antiferromagnetic systems. Low Temp. Phys. 2014; 40:17–35.

7. Jungwirth T, Marti X, Wadley P, Wunderlich J. Antiferromagnetic spintronics. Nat. Nanotech. 2016; 5:231–241.

8. Baltz V, et al. Antiferromagnetism: the next flagship magnetic order for spintronics? arXiv: 1606.04284.

9. N mec P, Fiebig M, Kampfrath T, Kimel AV. Antiferromagnetic opto-spintronics: Part of a collection of reviews on antiferromagnetic spintronics. arXiv:1705.10600.

10. Kahn FJ, Pershan PS, Remeika JP. Ultraviolet magneto-optical properties of single-crystal orthoferrites, garnets, and other ferric oxide compounds. Phys. Rev. 1969; 186:891–918.

11. Smolenskiĭ GA, Pisarev RV, Siniĭ IG. Birefringence of light in magnetically ordered crystals. Sov. Phys. -Usp. 1975; 18:410–429.

12. Zenkov AV, et al. Anisotropry of the Faraday effect in the weak ferromagnet $YFeO_3$. Zh. Eksp. Teor. Fiz. 1989; 96:1397. [JETP **69**, 792 (1989)].

13. Zubov VE, Krinchik GS, Seleznev VN, Strugatskii MB. Surface magnetism of iron borate. Zh. Eksp. Teor. Fiz. 1988; 94:290. [JETP **67**, 2122 (1988)].

14. Eremenko, VV., Kharchenko, NF., Litvinenko, YG., Naumenko, VM. Magneto-Optics and Spectroscopy of Antiferromagnets. Springer-Verlag; New York: 1992.

15. Nakatsuji S, Kiyohara N, Higo T. Large anomalous Hall effect in a non-collinear antiferromagnet at room temperature. Nature. 2015; 527:212–215. [PubMed: 26524519]

16. Suzuki M-T, Koretsune T, Ochi M, Arita R. Cluster multipole theory for anomalous Hall effect in antiferromagnets. Phys. Rev. B. 2017; 95:094406.

17. Argyres PN. Theory of the Faraday and Kerr Effects in Ferromagnetics. Phys. Rev. 1955; 97:334–345.

18. Erskine JL, Stern EA. Magneto-optic Kerr Effect in Ni, Co, and Fe. Phys. Rev. Lett. 1973; 30:1329–1332.

19. Oppeneer, PM. Magneto-Optical Kerr Spectra in. In: Buschow, KHJ., editor. Handbook of Magnetic Materials. Vol. 13. Elsevier; Amsterdam: 2001. p. 229-422.

20. Kimel AV, Kirilyuk A, Tsvetkov A, Pisarev RV, Rasing T. Laser-induced ultrafast spin reorientation in the antiferromagnet $TmFeO_3$. Nature. 2004; 429:850–853. [PubMed: 15215858]

21. Kimel AV, et al. Optical excitation of antiferromagnetic resonance in $TmFeO_3$. Phys. Rev. B. 2006; 74:060403(R).

22. Kalashnikova AM, et al. Impulsive excitation of coherent magnons and phonons by subpicosecond laser pulses in the weak ferromagnet $FeBO_3$. Phys. Rev. B. 2008; 78:104301.

23. Saidl V, et al. Optical determination of the Néel vector in a CuMnAs thin-film antiferromagnet. Nat. Photon. 2017; 11:91–96.

24. Nagaosa N, Sinova J, Onoda S, MacDonald AH, Ong NP. Anomalous Hall effect. Rev. Mod. Phys. 2010; 82:1539–1592.

25. Shindou R, Nagaosa N. Orbital ferromagnetism and anomalous Hall effect in antiferromagnets on the distorted fcc lattice. Phys. Rev. Lett. 2001; 87:116801. [PubMed: 11531542]

26. Machida Y, Nakatsuji S, Onoda S, Tayama T, Sakakibara T. Time-reversal symmetry breaking and spontaneous Hall effect without magnetic dipole order. Nature. 2010; 463:210–213. [PubMed: 20010605]

27. Chen H, Niu Q, MacDonald AH. Anomalous Hall effect arising from noncollinear antiferromagnetism. Phys. Rev. Lett. 2014; 112:017205. [PubMed: 24483927]

28. Kiyohara N, Tomita T, Nakatsuji S. Giant Anomalous Hall Effect in the Chiral Antiferromagnet Mn_3Ge. Phys. Rev. Applied. 2016; 5:064009.

29. Nayak AK, et al. Large anomalous Hall effect driven by a nonvanishing Berry curvature in the noncolinear antiferromagnet Mn_3Ge. Sci. Adv. 2016; 2:e1501870. [PubMed: 27152355]

30. Ikhlas M, et al. Large anomalous Nernst effect at room temperature in a chiral antiferromagnet. Nat. Phys. 2017

31. Feng W, Guo G-Y, Zhou J, Yao Y, Niu Q. Large magneto-optical Kerr effect in noncollinear antiferromagnets Mn_3X (X = Rh, Ir, Pt). Phys. Rev. B. 2015; 92:144426.

32. Krén E, Paitz J, Zimmer G, Zsoldos É. Study of the magnetic phase transformation in the Mn_3Sn phase. Physica B+C. 1975; 80:226–230.

33. Tomiyoshi S, Yamaguchi Y. Magnetic structure and weak ferromagnetism of Mn_3Sn studied by polarized neutron diffraction. J. Phys. Soc. Jpn. 1982; 51:2478–2486.

34. Nagamiya T, Tomiyoshi S, Yamaguchi Y. Triangular spin configuration and weak ferromagnetism of Mn_3Sn and Mn_3Ge. Solid State Commun. 1982; 42:385–388.

35. Manyala N, et al. Large anomalous Hall effect in a silicon-based magnetic semiconductor. Nat. Mater. 2004; 3:255–262. [PubMed: 15034565]

36. Solovyev IV. Magneto-optical effect in the weak ferromagnets LaMO$_3$ (M = Cr, Mn, and Fe). Phys. Rev. B. 1997; 55:8060–8063.

37. Liu J, Balents L. Anomalous Hall effect and topological defects in antiferromagnetic Weyl semimetals: Mn_3Sn/Ge. Phys. Rev. Lett. 2017; 119:087202. [PubMed: 28952754]

38. Yang H, et al. Topological Weyl semimetals in the chiral antiferromagnetic materials Mn_3Ge and Mn_3Sn. New J. Phys. 2017; 19:015008.

39. Kuroda K, et al. Evidence for magnetic magnetic Weyl fermions in a correlated metal. Nat. Mater. 2017; 16:1090–1095. [PubMed: 28967918]

40. Kargarian M, Randeria M, Trivedi N. Theory of Kerr and Faraday rotations and linear dichroism in topological Weyl semimetals. Sci. Rep. 2015; 5:12683. [PubMed: 26235120]

41. Badoz J, Billardon M, Canit JC, Russel MF. Sensitive devices to determine the state and degree of polarization of a light beam using a birefringence modulator. J. Opt. 1977; 8:373.

42. Patankar S, et al. Resonant magneto-optic Kerr effect in the magnetic topological insulator Cr : (Sb$_x$, Bi$_{1−x}$)$_2$Te$_3$. Phys. Rev. B. 2015; 92:214440.

43. Perdew JP, Burke K, Ernzerhof M. Generalized gradient approximation made simple. Phys. Rev. Lett. 1996; 77:3865–3868. [PubMed: 10062328]

44. Giannozzi P, et al. QUANTUM ESPRESSO: a modular and open-source software project for quantum simulations of materials. J. Phys.: Condens. Matter. 2009; 21:395502. [PubMed: 21832390]

45. Vanderbilt D. Soft self-consistent pseudopotentials in a generalized eigenvalue formalism. Phys. Rev. B. 1990; 41:7892–7895.

46. Mostofi AA, et al. wannier90: A tool for obtaining maximally-localised Wannier functions. Computer Physics Communications. 2008; 178:685–699.

47. Zhu LJ, Pan D, Nie SH, Lu J, Zhao JH. Tailoring magnetism of multifunctional Mn_xGa films with giant perpendicular anisotropy. Appl. Phys. Lett. 2013; 102:132403.

48. Zhu LJ, Brandt L, Zhao JH, Woltersdorf G. Composition-tuned magneto-optical Kerr effect in L1$_0$-Mn_xGa films with giant perpendicular anisotropy. J. Phys. D: Appl. Phys. 2016; 49:245001.

49. Krishnan KM. Ferromagnetic δ-$Mn_{1−x}Ga_x$ thin films with perpendicular anisotropy. Appl. Phys. Lett. 1992; 61:2365–2367.

50. Kato T, Kikuzawa H, Iwata S, Tsunashima S, Uchiyama S. Magneto-optical effect in $MnPt_3$ alloy films. J. Magn. Magn. Mater. 1995; 140:713–714.

51. Di G-Q, Oikawa S, Iwata S, Tsunashima S, Uchiyama S. Kerr Rotation of Quenched High-Temperature-Phase MnBi Film. J. J. Appl. Phys. 1994; 33:L783.

52. Yamamoto S, Fujii T. Magnetic and magneto-optical properties of Sn-substituted Mn_2Sb films. IEEE Trans. J. Magn. Jpn. 1991; 6:862–868.

53. Buschow KHJ, van Engen PG, Jongebreur R. Magneto-optical properties of metallic ferromagnetic materials. J. Magn. Magn. Mater. 1983; 38:1–22.

54. Ohyama R, Koyanagi T, Matsubara K. Magneto-optical Kerr effect of rf-sputtered PtMnSb thin films. J. Appl. Phys. 1987; 61:2347–2352.

55. Mitani S, et al. Perpendicular magnetic anisotropy and magneto-optical Kerr rotation in FePt(001) monoatomic multilayers. J. Magn. Magn. Mater. 1995; 148:163–164.

56. Zhang X, Schoenes J, Wachter P. Kerr-effect and dielectric tensor elements of magnetite (Fe$_3$O$_4$) between 0.5 and 4.3 eV. Solid State Commun. 1981; 39:189–192.

57. Gilleo, MA. Ferromagnetic insulators: Garnets in. In: Wohlfarth, EP., editor. Handbook of Ferromagnetic Materials. Vol. 2. North-Holland Publishing Company; Amsterdam: 1980. p. 1-53.

58. Kahn FJ, Pershan PS, Remeika JP. Ultraviolet magneto-optical properties of single-crystal ferrimagnetic ferric oxide compounds. J. Appl. Phys. 1969; 40:1508–1510.

59. Visnovsky S, et al. Magnetooptical polar Kerr effect in ferrimagnetic garnets and spinels. IEEE Trans. Magn. 1981; 17:3205–3210.

60. Nielsen JW. Properties and preparation of magnetic materials for bubble domains. Met. Trans. 1971; 2:625–633.

61. Treves D. Studies on orthoferrites at the Weizmann institute of science. J. Appl. Phys. 1965; 36:1033–1039.

a

b

c

d
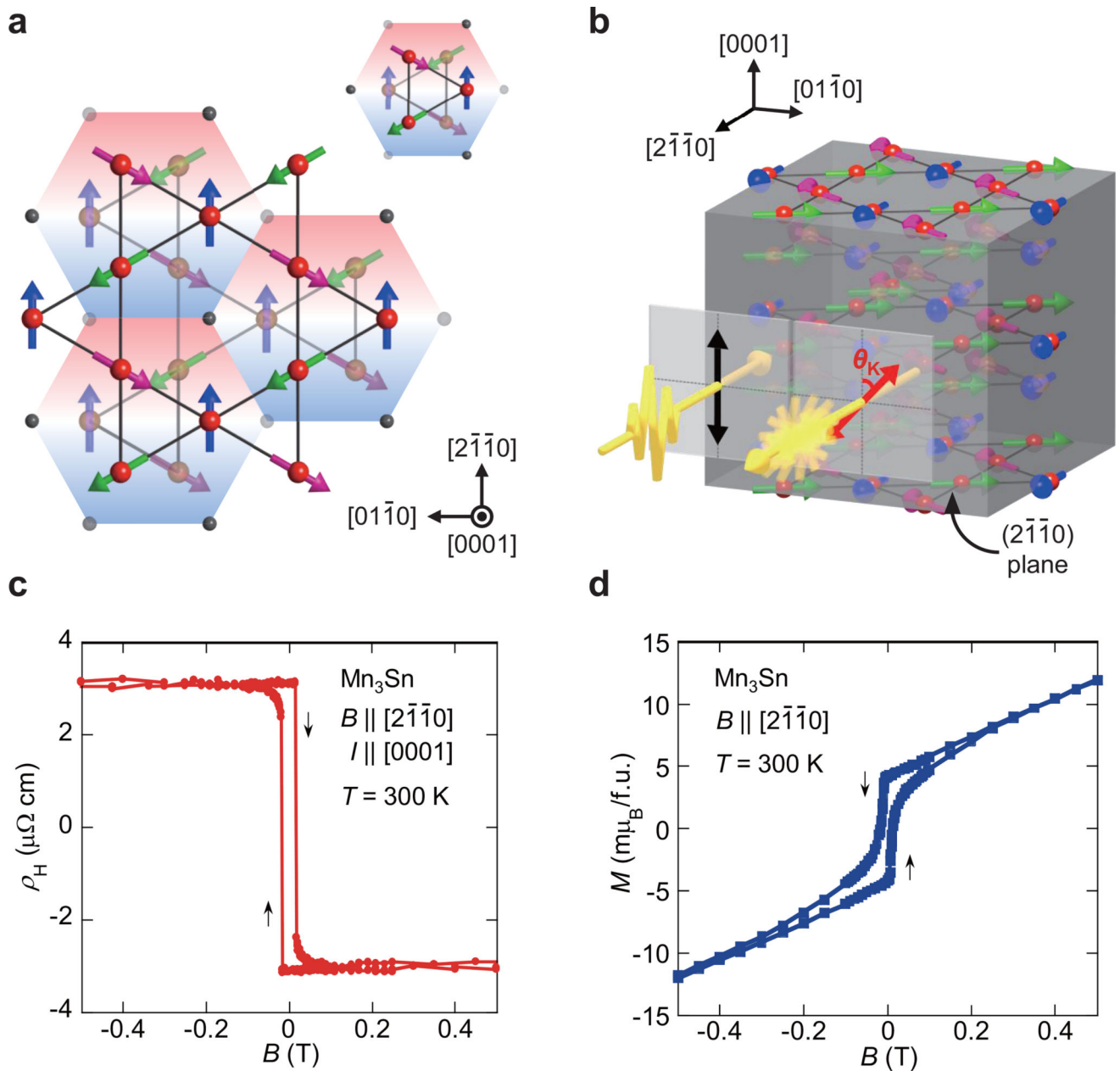
Figure 1. Crystal and magnetic structures, anomalous Hall effect and weak ferromagnetism at 300 K of the non-collinear antiferromagnet Mn₃Sn

a, Large red (small dark grey) and large transparent orange (small transparent grey) spheres represent Mn (Sn) atoms forming kagome planes at $z = 0$ and $1/2$, respectively. The Mn magnetic moments (arrows) lie in the (0001)-plane and form an inverse triangular spin structure. Different colours of arrows indicate three sublattices. The spin structure on the kagome bilayers can be considered as ferroic ordering of cluster magnetic octupoles by using the cluster octupole unit shown in the inset. **b**, Schematic illustration of magneto-optical Kerr effect measurements. A polarized light beam is applied perpendicular to the (2$\bar{1}\bar{1}$0)-plane, and the reflected light becomes elliptically polarized with the major axis

rotated by θ_K. **c,d** Field dependence of **c**, the Hall resistivity ρ_H in the magnetic field $B \parallel$ [$2\bar{1}\bar{1}0$] with the electric current $I \parallel$ [0001], and of **d**, the magnetization M in $B \parallel$ [$2\bar{1}\bar{1}0$].
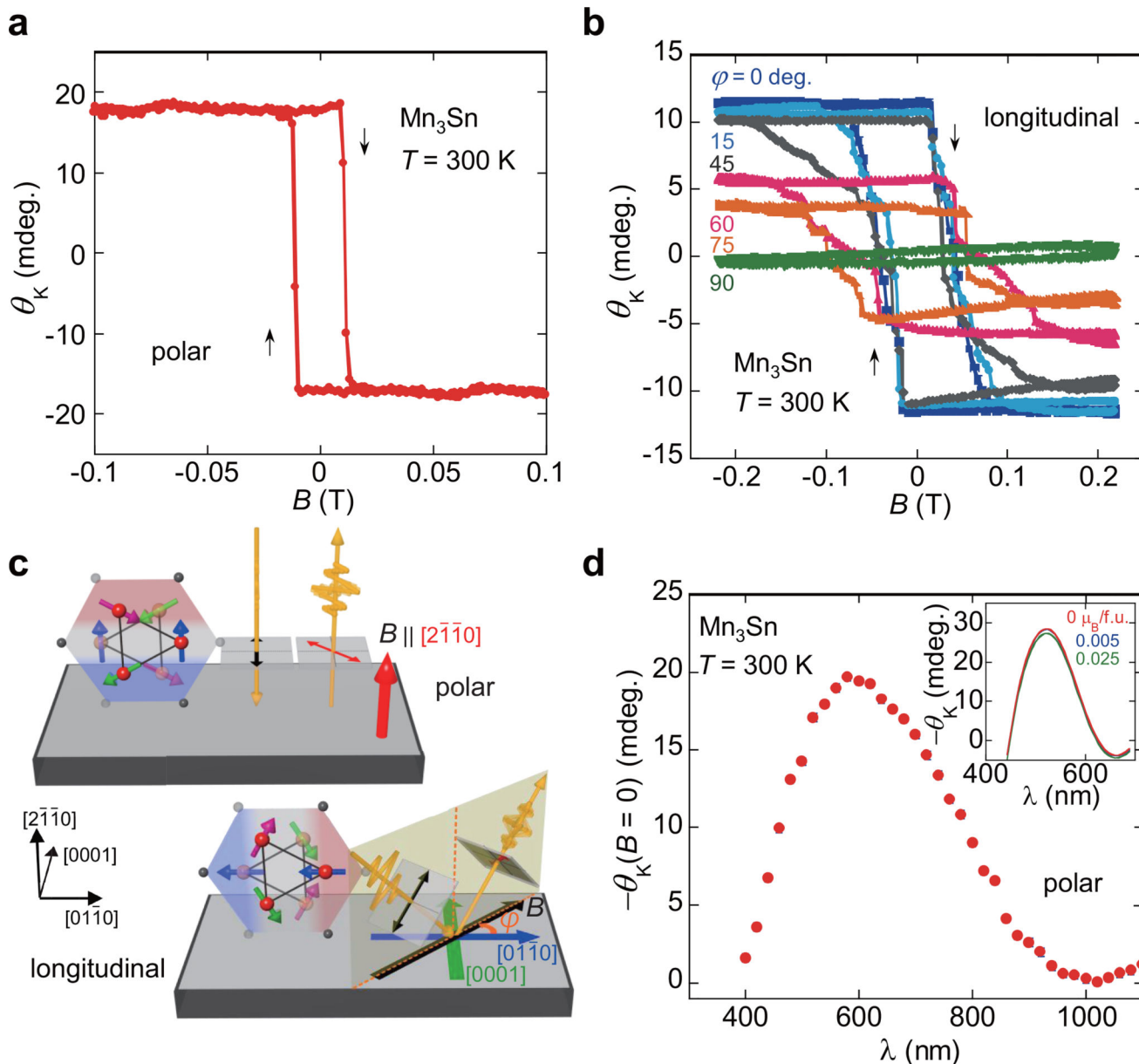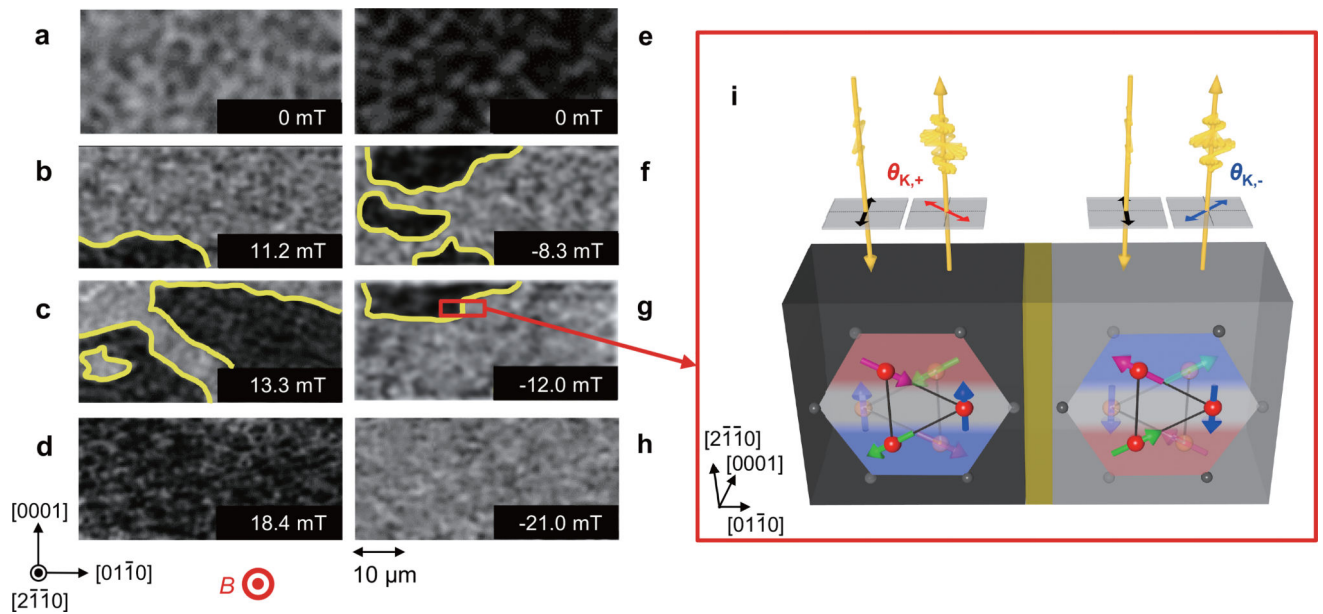
Figure 2. Magneto-optical Kerr rotation in the non-collinear antiferromagnet Mn$_3$Sn at 300 K
Field dependence of **a**, the polar magneto-optical Kerr rotation angle θ_K for the $(2\bar{1}\bar{1}0)$-plane in $B \parallel [2\bar{1}\bar{1}0]$, and **b**, the longitudinal magneto-optical Kerr rotation angle θ_K of the $(2\bar{1}\bar{1}0)$-plane measured along $\varphi = 0$–90 degrees (Methods). **c**, Schematic illustrations of sample configurations for the polar and longitudinal magneto-optical Kerr effects (MOKE) (Methods). **d**, Polar MOKE spectroscopy of the $(2\bar{1}\bar{1}0)$-plane from 400 nm to 1100 nm under zero magnetic field (Methods). Inset: Polar Kerr rotation spectrum obtained using the first-principles calculation with the smearing parameter of $\eta = 0.4$ eV (Methods). The rotation angle slightly changes with M, and there is almost no change in the angle between $M = 0$ and 0.005 μ_B/f.u. Since the observed M is just ~0.005 μ_B/f.u. (~0.002 μ_B/Mn), we may conclude that M plays just a minor role in the MOKE.
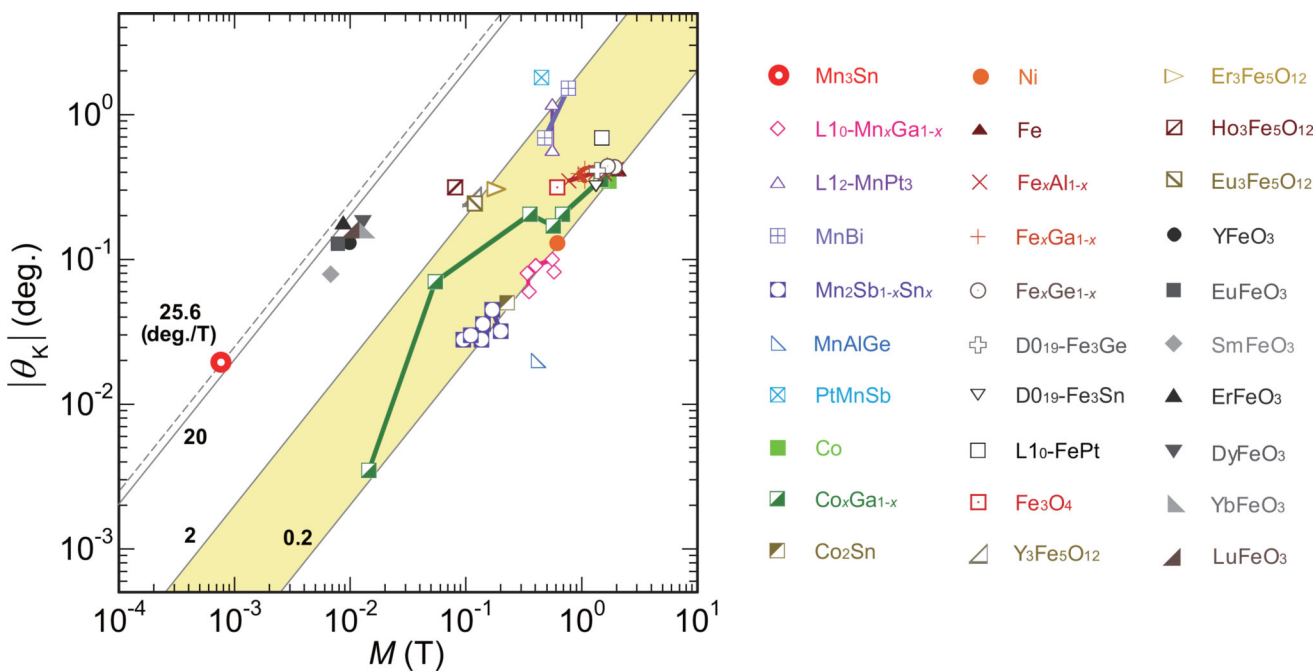
Figure 3. Magnetization dependence of the polar Kerr effect at room-temperature for ferroand ferrimagnets, and antiferromagnets including Mn$_3$Sn

Full logarithmic plot of the polar magneto-optical Kerr rotation angle $|\theta_K|$ vs. the magnetization M for various ferro- and ferrimagnets, and antiferromagnets including Mn$_3$Sn measured around room-temperature (Methods). Here, Mn$_3$Sn is the only non-collinear antiferromagnet even in its fully compensated antiferromagnetic state. In ferromagnetic systems, it shows a general trend for most of the ferro- and ferrimagnets that $|\theta_K|$ increases with increasing M, namely $|\theta_K| = K_S M$. Here, K_S is a coefficient, ranging between 0.2 and 2.0 degrees/T for ferro- and ferrimagnets, as highlighted by the shaded region. The spontaneous polar MOKE signal of Mn$_3$Sn does not follow the above scaling for ferromagnets and K_S has a 1–2 order(s) of magnitude larger value of 25.6 degrees/T, which is still the largest among antiferromagnets that have similar magnitude of $K_S = 10$–20 degrees/T.

Figure 4. Magneto-optical Kerr effect (MOKE) images in the non-collinear antiferromagnet Mn₃Sn

Evolution of the antiferromagnetic domains of the $(2\bar{1}\bar{1}0)$-plane as a function of a field B along $[2\bar{1}\bar{1}0]$ (-21 mT $\leq B \leq 21$ mT). The imaging area is 25 μm × 50 μm. Grey and black regions correspond to positive and negative values of the MOKE signal. **a–d**, MOKE images obtained in the increasing field process from -21 mT to 21 mT. **e–h**, MOKE images obtained in the decreasing field process from 21 mT to -21 mT. (i) Schematic illustration of two regions with different MOKE image contrasts (grey/black areas) due to opposite signs of the Kerr angles $\theta_{K,-/+}$, corresponding to two types of cluster magnetic octupole domains which have the inverse triangular spin structures with opposite spin directions within the (0001)-plane. The two regions should be separated by a domain wall (yellow area).